

Misfit Strain-Induced Buckling for Transition-Metal Dichalcogenide Lateral Heterostructures: A Molecular Dynamics Study

Jin-Wu Jiang

Acta Mechanica Solida Sinica
The Chinese Society of Theoretical and Applied Mechanics

ISSN 0894-9166

Acta Mech. Solida Sin.
DOI 10.1007/s10338-018-0049-z



 Springer

Your article is protected by copyright and all rights are held exclusively by The Chinese Society of Theoretical and Applied Mechanics and Technology. This e-offprint is for personal use only and shall not be self-archived in electronic repositories. If you wish to self-archive your article, please use the accepted manuscript version for posting on your own website. You may further deposit the accepted manuscript version in any repository, provided it is only made publicly available 12 months after official publication or later and provided acknowledgement is given to the original source of publication and a link is inserted to the published article on Springer's website. The link must be accompanied by the following text: "The final publication is available at link.springer.com".



Misfit Strain-Induced Buckling for Transition-Metal Dichalcogenide Lateral Heterostructures: A Molecular Dynamics Study

Jin-Wu Jiang^{1*}

(¹*Shanghai Key Laboratory of Mechanics in Energy Engineering, Shanghai Institute of Applied Mathematics and Mechanics, Shanghai University, Shanghai 200072, China*)

Received 24 April 2018; revision received 8 August 2018; Accepted 9 August 2018

© The Chinese Society of Theoretical and Applied Mechanics and Technology 2018

ABSTRACT Molecular dynamics simulations are performed to investigate the misfit strain-induced buckling of the transition-metal dichalcogenide (TMD) lateral heterostructures, denoted by the seamless epitaxial growth of different TMDs along the in-plane direction. The Stillinger–Weber potential is utilized to describe both the interaction for each TMD and the coupling between different TMDs, i.e., MX₂ (with M = Mo, W and X = S, Se, Te). It is found that the misfit strain can induce strong buckling of the freestanding TMD lateral heterostructures of large area, resulting from the TMDs' atomic-thick nature. The buckling phenomenon occurs in a variety of TMD lateral heterostructures of different compositions and in various patterns. Our findings raise a fundamental mechanical challenge for the structural stability of the freestanding TMD lateral heterostructures.

KEY WORDS Transition-metal dichalcogenide, Lateral heterostructure, Stillinger–Weber potential, Molecular dynamics simulation

1. Introduction

The layered transition-metal dichalcogenides (TMDs) have attracted considerable attention as semiconductors with tunable electronic and other distinctive electro-optical properties. The growth of TMDs in the form of lateral heterostructures is a powerful technique to construct lateral p-n diodes with excellent current rectification and other functional devices based on the TMDs. In 2014, several experiments successfully fabricated the TMD lateral heterostructures and illustrated some novel properties. The WSe₂–MoSe₂ lateral heterostructure was produced by using a mixture of WSe₂ and MoSe₂ powders as the source for the chemical vapor deposition (CVD) process [1]. The WS₂–WSe₂ lateral heterostructure was synthesized by controlling the growth temperature, where atomic visualization discloses the preference of the lateral interface along the zigzag direction [2]. Another experiment also revealed the zigzag direction to be the preferable growth direction for the lateral interface [3]. Duan et al. synthesized the MoS₂–MoSe₂ and WS₂–WSe₂ lateral heterostructures by in situ modulation of the reactants during the CVD growth process, where the synthetic conditions are kept unchanged during the switch of the reactants, so that the edge is fresh and unpassivated and can serve as the active growth front for successive lateral epitaxial growth [4].

* Corresponding author. E-mail: jiangjinwu@shu.edu.cn; jwjiang5918@hotmail.com

In the past few years, considerable efforts have been made to improve the growth of the TMD lateral heterostructure. Various modified CVD techniques were introduced to synthesize TMD lateral heterostructures, aiming mainly at more precise control over patterns and sharper lateral interface [5–14]. Li et al. developed a two-step epitaxial growth of the seamless WSe₂–MoS₂ lateral heterostructure (of different metals and chalcogen) with atomically sharp lateral interfaces, through proper control over the CVD conditions to avoid possible alloy reactions [15]. Recently, Zhang et al. designed a robust step-by-step CVD process to grow diverse TMD lateral heterostructures with multiple distinct TMD blocks, by preventing undesired thermal degradation and uncontrolled homogeneous nucleation [16]. Experiments have revealed some important mechanisms that can affect the synthesis of the TMD lateral heterostructures, such as the diffusion mechanism[17] and the layer number [18]. Though TMD lateral heterostructures have been mostly grown by the CVD method, the lithography technique has been used to assist the creation of TMD lateral heterostructures in predefined patterns [19, 20], and the pulsed-laser-deposition-assisted selenization method was used to grow the MoSe₂–WSe₂ lateral heterostructure [21]. Besides the two-phase heterostructures, some other TMD lateral structures with tunable properties have also been synthesized in recent years, such as the TMD alloys with randomly distributed composition (e.g., Mo_{1-x}W_xS₂) [22–28] or spatially graded composition [29–32].

As a characteristic feature of the coherent interface, the misfit strain plays an important role in physical properties of the interface in TMD lateral heterostructures. By growing TMD coherent lateral heterostructures with controlled supercell dimensions, Xie et al. illustrated the tunability of optical properties by the misfit strain [33]. Zhang et al. measured the distribution of the misfit strain tensor by examining the Moire pattern and investigated the misfit strain effect on the band alignment of the WSe₂–MoS₂ lateral heterostructures [34]. From the mechanics point of view, TMDs are atomic membranes of high flexibility, so these structures are easy to buckle under compression. The misfit will cause compressive stress in the TMD of larger lattice constant in the lateral heterostructure, where the buckling instability may take place. This misfit strain-induced buckling has been discussed for the graphene and boron nitride lateral heterostructure [35]. The possibility of this misfit strain-induced buckling is thus one of the topics discussed in the present work.

Although experiments have gained significant progress on synthesizing TMD lateral heterostructures, present theoretical studies are quite limited and mostly focus on the electronic band alignment for TMD alloys [26, 36] or TMD lateral heterostructures [37–43], the electronic transport properties [44–47], or some possible applications [48, 49]. Few studies investigated the possibility of designing lateral heterostructures by the first-principles calculations [50–57]. All of these theoretical studies are based on the first-principles calculations approach, which is accurate but of expensive computational costs. Theoretical investigations are needed for many emerging mechanical or thermal properties of the TMD lateral heterostructures, such as the distribution of the misfit strain, the thermal transport across the lateral interface, the sharpness of the lateral interface. These properties are sensitive to the size of the structure and typically require more than tens of thousands of atoms, which is out of the capability of first-principles calculations. An empirical potential is thus highly desirable for these investigations, which will be developed in the present work.

In this work, we perform molecular dynamics simulations to study the misfit strain-induced buckling in the TMD lateral heterostructures. The Stillinger–Weber (SW) potential is used to describe both the interaction within each TMD and the coupling between different TMDs. We calculate the strain distribution within the TMD lateral heterostructure, and the results are consistent with the experiment. Misfit strain can cause the buckling of TMD lateral heterostructures with the size larger than a critical value, due to the atomic-thick nature of the TMD layers. The misfit strain-induced buckling is found to be a general phenomenon in TMD lateral heterostructures constructed by different TMD constitutions or of different patterns.

2. Simulation Details

The SW potential is one of the most efficient nonlinear empirical potentials and will be used to describe the interaction for TMD lateral heterostructures in the present work. It contains the following two-body and three-body interaction terms,

$$V_2(r_{ij}) = \epsilon A (B\sigma^p r_{ij}^{-p} - \sigma^q r_{ij}^{-q}) e^{[\sigma(r_{ij} - a\sigma)^{-1}]} \quad (1)$$

$$V_3(\vec{r}_i, \vec{r}_j, \vec{r}_k) = \epsilon \lambda e^{[\gamma\sigma(r_{ij} - a\sigma)^{-1} + \gamma\sigma(r_{jk} - a\sigma)^{-1}]} (\cos\theta_{jik} - \cos\theta_0)^2 \quad (2)$$

where r_{ij} is the distance between atoms i and j , and θ_{jik} is the angle formed by bonds r_{ji} and r_{jk} . θ_0 is the equilibrium bond angle. Other quantities are SW potential parameters to be parametrized for different materials. We have recently parameterized the SW potential for most atomic-thick-layered materials including individual TMDs, i.e., MX_2 (with $\text{M} = \text{Mo}, \text{W}$ and $\text{X} = \text{S}, \text{Se}, \text{Te}$) [58].

There are two inequivalent bond angles in the hexagonal MX_2 , which, however, are very close to each other for MX_2 with $\text{M} = \text{Mo}, \text{W}$ and $\text{X} = \text{S}, \text{Se}, \text{Te}$. For example, these two inequivalent angles are 82.119° and 81.343° in MoSe_2 [58]. We can thus simplify the configuration of the MX_2 by using a single bond angle $\theta_0 = 80.581^\circ$. This simplification gives reasonably accurate results for MoS_2 [59]. The simplification is applicable to MX_2 with $\text{M} = \text{Mo}, \text{W}$ and $\text{X} = \text{S}, \text{Se}, \text{Te}$ and is adopted in the present work.

In the TMD lateral heterostructures, there are crossing interactions between two TMDs, where new terms of the three-body form in Eq. (2) are needed. Let's take $\text{MoS}_2\text{--WSe}_2$ lateral heterostructure as an example. At the interface, there are crossing angles like θ_{MoSe} , which can be regarded as the substitution of one S atom by the Se atom in the angle θ_{MoSS} , as illustrated in Fig. 1. We focus on the angle $\theta_{\text{MoS}_1\text{S}_4}$ (with Mo as the apex). The substitution of S_1 atom by Se atom in Fig. 1 can cause two competing effects on the equilibrium value of angle $\theta_{\text{MoS}_1\text{S}_4} = \theta_0$. First, Se has a larger nuclear radius than S (i.e., Se has more electrons than S), so the repulsive force between Se– S_4 is stronger than $\text{S}_1\text{--S}_4$, which shall enlarge the equilibrium angle θ_0 . Second, the Se atom is further away from the Mo atom (i.e., Mo–Se bond is longer than Mo–S bond), which tends to reduce the value of angle θ_0 . These two competing effects cancel with each other, resulting in only neglectable changes of the equilibrium angle θ_0 . It is thus reasonable to assume that the equilibrium angle $\theta_0 = 80.581^\circ$ keeps unchanged in the crossing angles like θ_{MoSeS_4} . We thus use $\theta_0 = 80.581^\circ$ for all bond angles in the TMD lateral heterostructures. It should be noted that the bending of angles like $\theta_{\text{MoS}_1\text{S}_6}$ is not considered in the SW potential, and a modification is necessary for LAMMPS to exclude this term in the three-body SW potential (see “Appendix”).

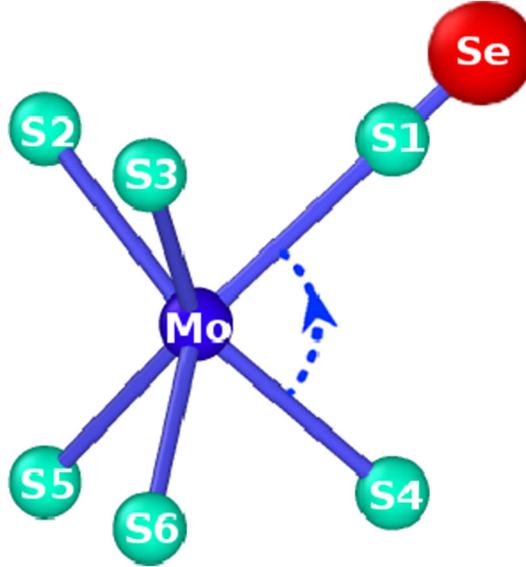


Fig. 1. (Color online) Local environment around atom Mo in the MoS_2 hexagonal lattice with the Mo layer sandwiched by two S layers. Atoms S_1, S_2 , and S_3 are in the top group of the MoS_2 layer. Atoms S_4, S_5 , and S_6 are in the bottom group of the MoS_2 layer. Atom S_1 is substituted by atom Se. Note that the bending of angles like $\theta_{\text{MoS}_1\text{S}_6}$ is not considered in the SW potential, and a modification is necessary for LAMMPS to exclude this term in the three-body SW potential (see “Appendix”)

The energy parameter $\lambda_{MXM'}$ in Eq. (2) for the crossing angle $\theta_{MXM'}$ is derived by the geometric average,

$$\lambda_{MXX'} = \sqrt{\lambda_{MXX}\lambda_{MX'X'}} \quad (3)$$

where λ_{MXX} and $\lambda_{MX'X'}$ are angle bending parameters corresponding to θ_{MXX} and $\theta_{MX'X'}$ in the individual TMD, respectively [58]. There is no new term of the two-body form. We have generated all necessary terms for the SW potential of the multicomponent MX_2 system with $M = Mo, W$ and $X = S, Se, Te$. The SW potential script for LAMMPS can be found from our group Web site <http://jiangjinwu.org/sw>. Specifically, this SW potential script is applicable to various TMD compounds, such as alloys and lateral heterostructures. We note that the largest system simulated in the present work contains more than 50,000 atoms, which goes beyond the computational capability of first-principles approaches and thus exhibits the power of the SW empirical potential.

Molecular dynamics simulations are performed to simulate the TMD lateral heterostructures. The TMD lateral heterostructures are first relaxed to the energy-minimum configuration by the conjugate gradient (CG) algorithm. The relaxed structure is further thermalized within the NPT (constant particle number, constant pressure, and constant temperature) ensemble for 100 ps by the Nosé-Hoover approach [60, 61]. A low temperature of 4.2 K is used, so that the thermal expansion effect is neglectable and the buckling is intrinsically caused by the misfit strain. The thermal vibration becomes stronger at higher temperature, which shall increase the possibility of buckling. The standard Newton equations of motion are integrated in time using the velocity Verlet algorithm with a time step of 1 fs. Simulations are performed using the publicly available simulation code LAMMPS [62], while the OVITO package is used for visualization [63].

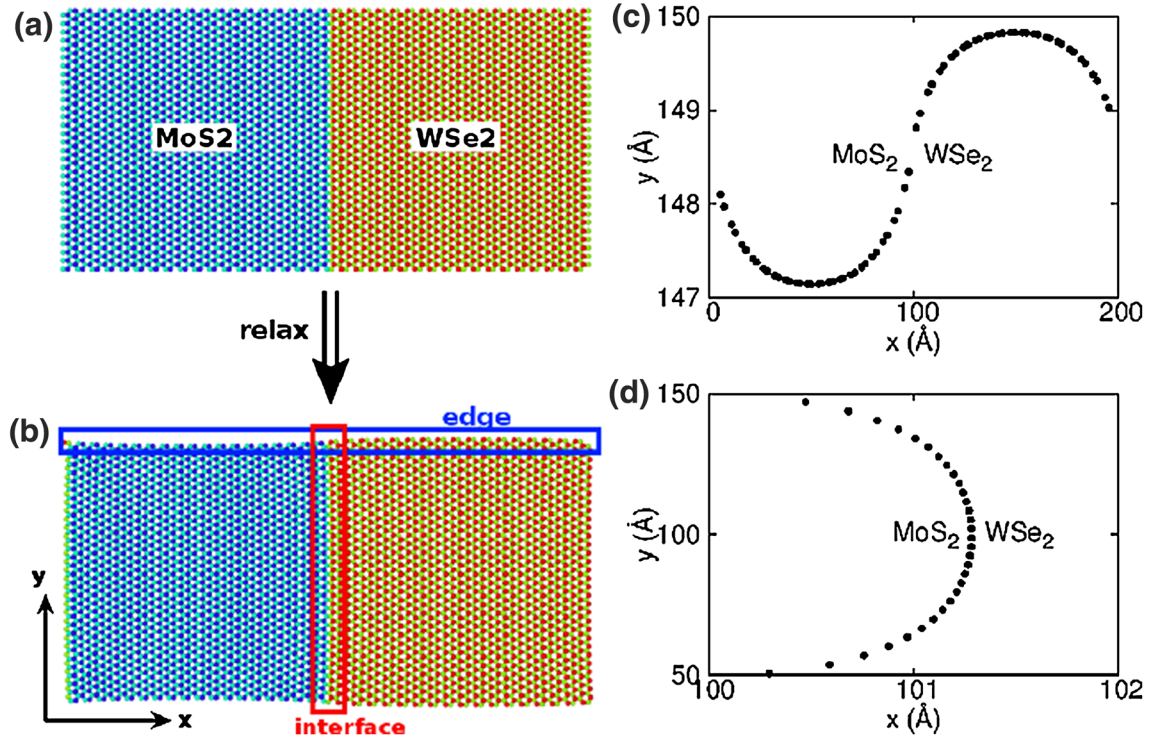


Fig. 2. (Color online) Configuration of the MoS₂-WSe₂ lateral heterostructure of dimension $L_x \times L_y = 200 \times 100 \text{ \AA}$. **a** Ideal unrelaxed structure. **b** Relaxed structure. The top edge (blue box) and the interface (red box) are deformed. **c** Details for the deformation of the top edge. **d** Details for the deformed interface illustrate the bending of the interface with MoS₂(WSe₂) on the inner (outer) side

3. Results and Discussions

Figure 2 shows the configuration for the MoS₂–WSe₂ lateral heterostructure of dimension $L_x \times L_y = 200 \times 100 \text{ \AA}$. The dimension in the z -direction (i.e., thickness) is not well defined in the atomic-thick nanomaterials. The thickness can be defined either as the space between two layers in the bulk system or as the size of the atom. However, this quantity is not used in the calculations of the present work, so we will not give an exact value for this quantity. MoS₂ is on the left while WSe₂ is on the right, forming a vertical interface in the middle. The interface is of the preferred zigzag shape as observed in the experiment [2, 3]. Figure 2a shows the ideal configuration, where MoS₂ and WSe₂ are constructed with a common lattice constant. The ideal configuration is relaxed to the energy-minimum state as shown in Fig. 2b. Periodic boundary condition is applied in the x -direction, and free boundary condition is applied in the y - and z -directions. The lattice constant of WSe₂ is larger than MoS₂, resulting in obvious misfit strain at the interface. The heterostructure is deformed by the misfit strain. Figure 2c is the enclosed configuration for the top edge. MoS₂ is stretched at the left side of interface, while WSe₂ is compressed at the right side of the interface, leading to the compressive (tensile) stress on the left

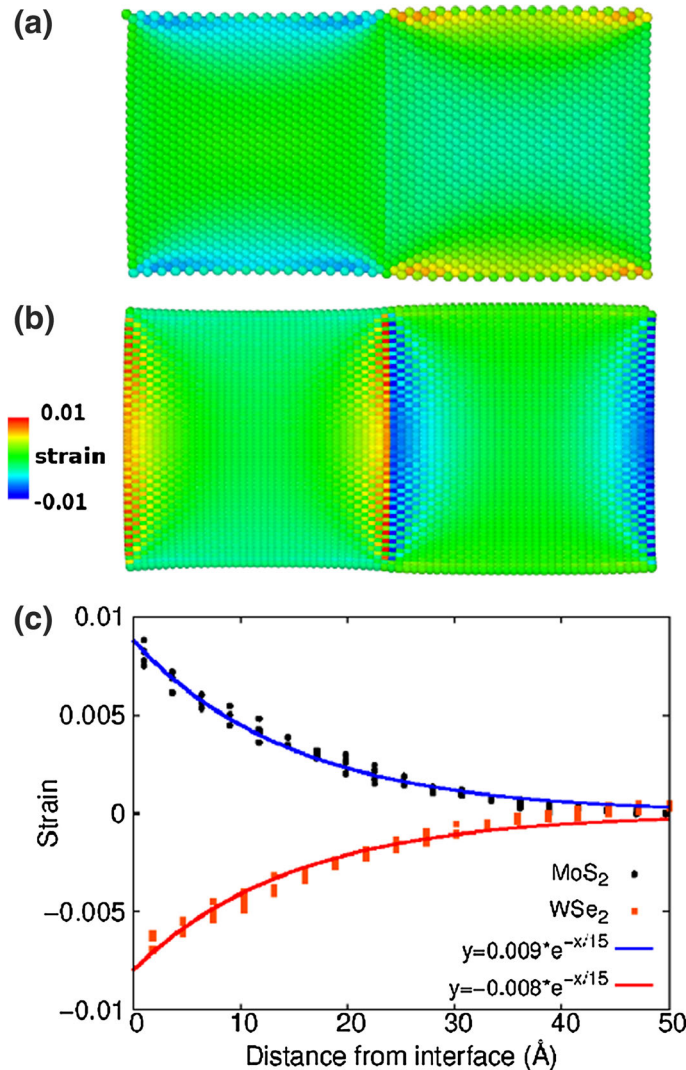


Fig. 3. (Color online) Strain distribution within the relaxed configuration of MoS₂–WSe₂ lateral heterostructure of dimension $L_x \times L_y = 200 \times 100 \text{ \AA}$. a Strain for bonds perpendicular to the interface. b Strain for bonds not perpendicular to the interface. c Strain versus the distance away from the central interface for atoms with $y = L_y/2$

(right) side of the interface. As a result, the interface is slightly bent with MoS₂(WSe₂) on the inner (outer) side as shown in Fig. 2d.

We further examine the strain distribution in Fig. 3 for the MoS₂–WSe₂ lateral heterostructure of dimension $L_x \times L_y = 200 \times 100 \text{ \AA}$. Figure 3a shows the strain distribution for bonds perpendicular to the interface. For the MoS₂ on the left of the interface, there is only small tensile strain in the interior region, and the top and bottom edges of the MoS₂ region are compressed due to the bending of the interface displayed in Fig. 2d (with MoS₂ on the inner side). For the WSe₂ on the right of the interface, there is small compressive strain in the interior region, and there are some tensile strains at the top and bottom edges due to the bending of the interface displayed in Fig. 2d (with WSe₂ on the outer side). Figure 3b illustrates the strain distribution for these bonds that are not perpendicular to the interface. Large strains are found at the middle interface. There is another interface formed by the left and right ends, due to the periodic boundary condition applied in the x -direction. We will focus on the interface at the middle of the system, i.e., at $x = L_x/2$. The strain decays rapidly away from the interface. Figure 3c is the strain versus distance from the interface for atoms at $y = L_y/2$. Both strains in MoS₂ (tensile) and WSe₂ (compressive) decay exponentially with a critical length of 15.0 \AA . The exponential decay of the strain was also observed in a recent experiment [34]. The strain for bonds perpendicular to the interface is much smaller than the strain for bonds not perpendicular to the interface, which is consistent with the experiment [33].

A particularly interesting result of Fig. 3c is a relatively large compressive strain (-0.8%) at the WSe₂ side of the interface. In contrast to the bulk epitaxial heterostructures, TMDs are atomic-thick with very small bending modulus, so the misfit strain-induced compression effect may induce buckling instability of the TMDs. There is no buckling phenomenon in the MoS₂–WSe₂ lateral heterostructure with $L_x = 200 \text{ \AA}$ and $L_y = 100 \text{ \AA}$ as discussed in Figs. 2 and 3. The misfit strain-induced stress at

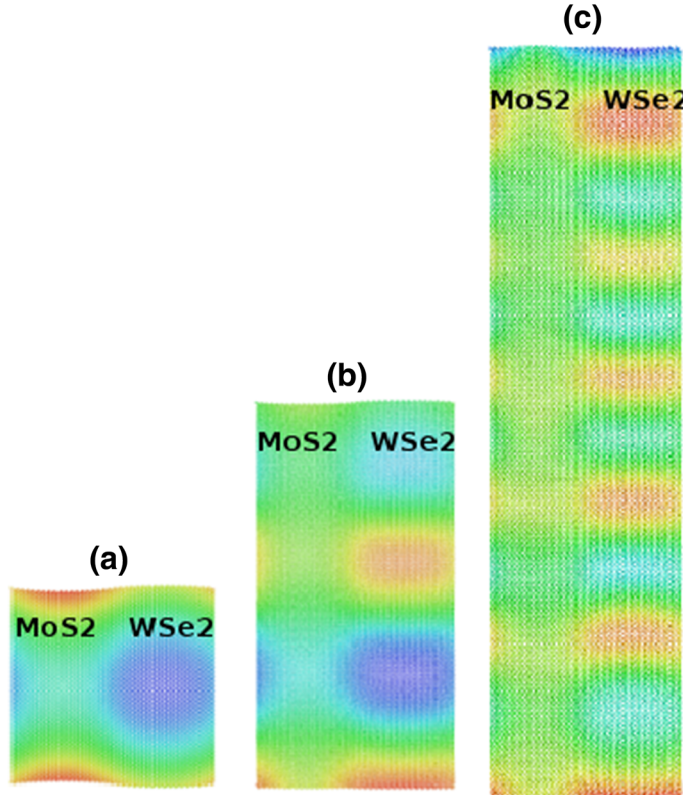


Fig. 4. (Color online) Buckling of the MoS₂–WSe₂ lateral heterostructure of length $L_x = 200 \text{ \AA}$ at 4.2 K. The width is $L_y = 200, 400, 800 \text{ \AA}$ for the structures shown in a, b and c, respectively. The WSe₂ in the right part buckles. Color represents the atomic z -coordinate

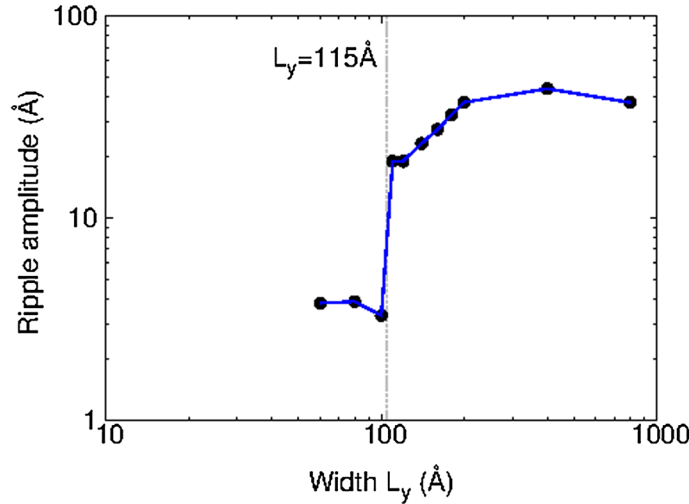


Fig. 5. (Color online) The amplitude of the buckling ripple for MoS₂–WSe₂ lateral heterostructure of different width L_y at 4.2 K. The length is fixed at $L_x = 200$ Å. The vertical gray line locates the critical width $L_y = 105$ Å, above which buckling occurs

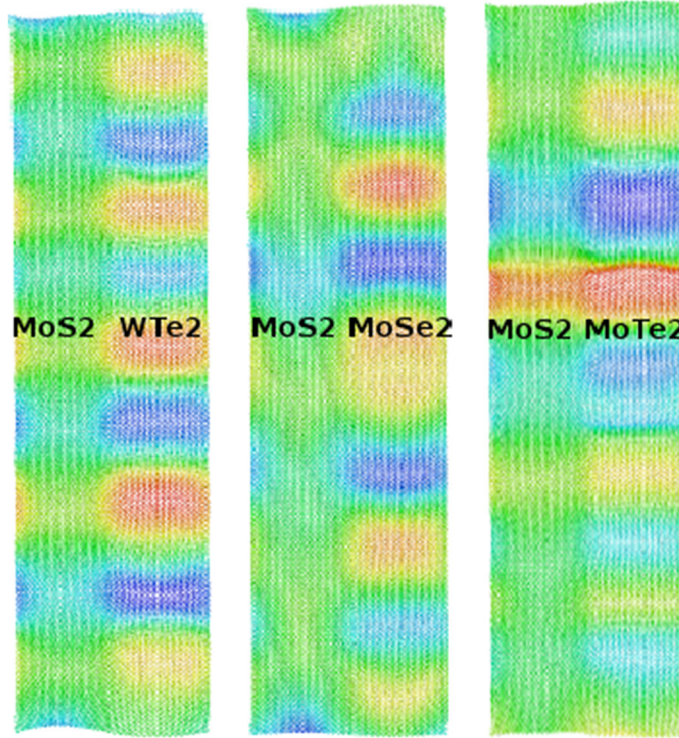


Fig. 6. (Color online) Misfit strain-induced buckling phenomenon in other TMD lateral heterostructures at 4.2 K. Systems from left to right are: MoS₂–WTe₂, MoS₂–MoSe₂, and MoS₂–MoTe₂. Color represents the atomic z-coordinate

the interface is along the y -direction, so we study more systems with larger L_y . We clearly observe buckling instability for TMD lateral heterostructures of larger L_y . Figure 4 illustrates the snapshots for typical buckling shapes of the WSe₂ on the right side of the interface for the MoS₂–WSe₂ lateral heterostructures with $L_y = 200, 400$, and 800 Å. Figure 5 reveals a critical value of $L_y = 105$ Å for the L_y dependence of the ripple amplitude. The ripple amplitude in Fig. 5 is estimated by $(z_{\max} - z_{\min})$, with z_{\max} and z_{\min} as the maximum and minimum values of the atomic z -coordinate, respectively. For systems with $L_y < 105$ Å, the ripple amplitudes are around a small value of 3.5 Å which essentially represents the thickness of the TMD layer. For structures with $L_y > 105$ Å, the ripple amplitude is considerably large, reflecting the buckling deformation of the TMD layer. It has been shown that the buckling of TMD layers will have obvious effects on the electronic transport properties [64]. Hence, these buckling patterns induced by the misfit strain can be applied as a valuable approach to tune electronic properties of the TMD lateral heterostructure.

There is also similar misfit strain-induced buckling instability in other TMD lateral heterostructures. Figure 6 shows the optimized configuration of the MoS₂–WTe₂, MoS₂–MoSe₂, and MoS₂–MoTe₂ lateral heterostructures of dimension $L_x \times L_y = 200 \times 800$ Å. Similar buckling phenomena occur in the TMDs with larger lattice constants, where the misfit-induced strain is compressive.

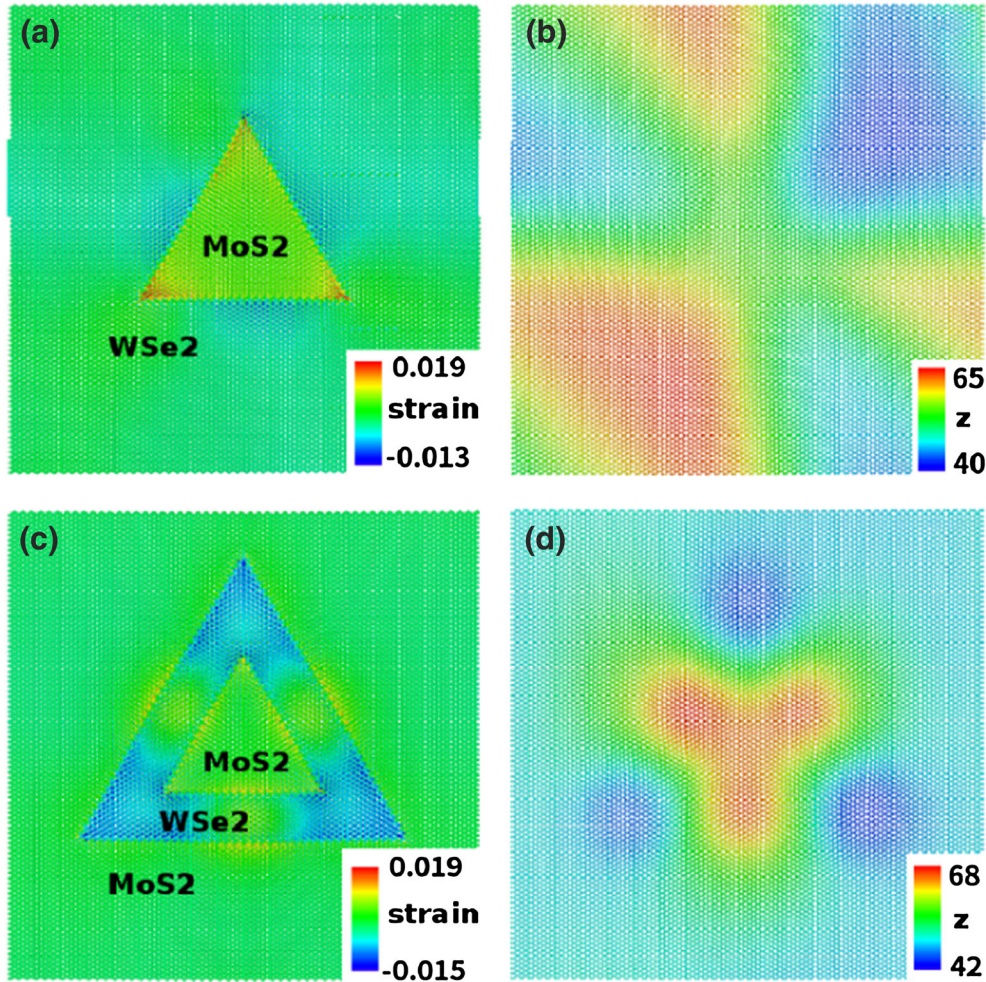


Fig. 7. (Color online) Misfit strain-induced buckling for TMD lateral heterostructures of triangular pattern at 4.2 K. **a** Strain distribution for MoS₂–WSe₂ lateral heterostructure, with the buckling shape shown in **b**. **c** Strain distribution for MoS₂–WSe₂–MoS₂ lateral heterostructure, with the buckling shape shown in **d**. Color corresponds to the strain in **a** and **c**, while color represents the z -coordinate in Å for **b** and **d**

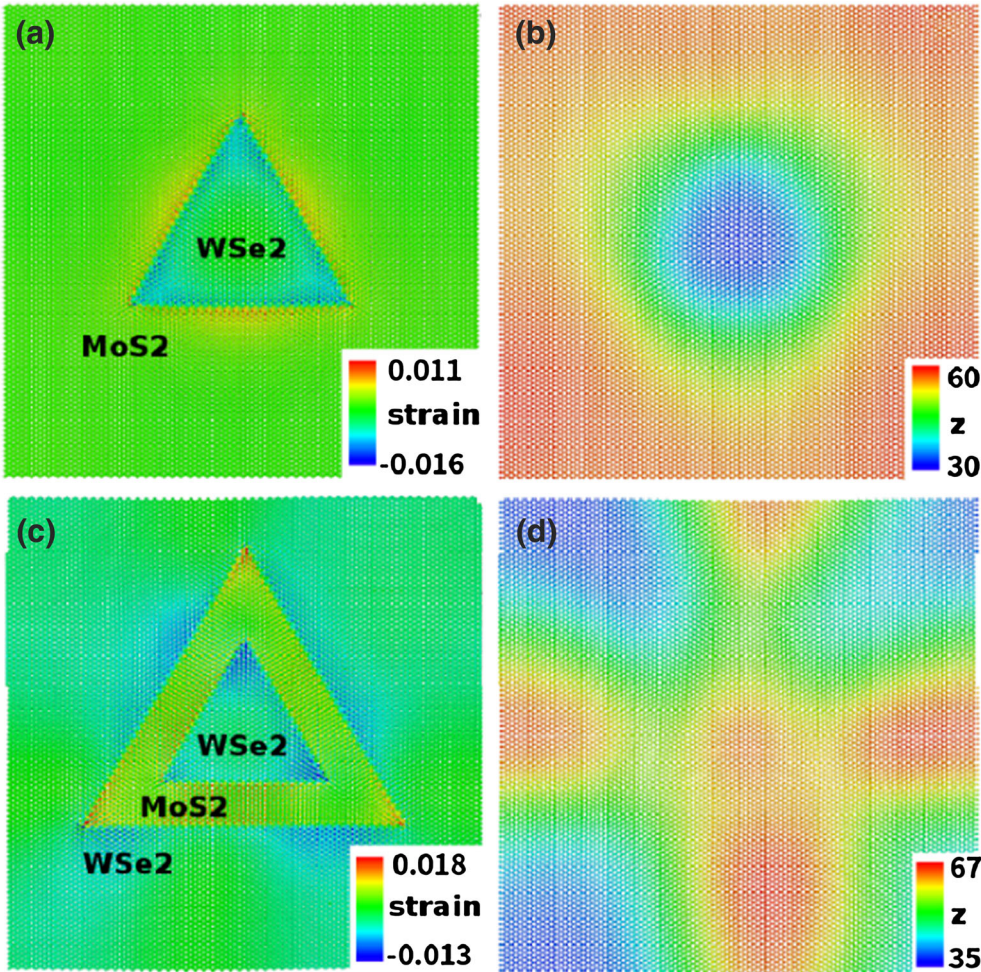


Fig. 8. (Color online) Misfit strain-induced buckling for the TMD lateral heterostructures of triangular pattern at 4.2 K. The constitutions are switched as compared with the system shown in Fig. 7. **a** Strain distribution for WSe₂–MoS₂ lateral heterostructure, with the buckling pattern shown in **b**. **c** Strain distribution for WSe₂–MoS₂–WSe₂ lateral heterostructure, with the buckling pattern shown in **d**. Color corresponds to the strain for **a** and **c**, while color represents the z-coordinate in Å for **b** and **d**

In the above, we have investigated the TMD lateral heterostructures in the rectangular pattern. Experiments have frequently grown the TMD lateral heterostructures of triangular patterns, resulting from the threefold rotational symmetry of the TMDs. We thus study the misfit strain-induced buckling of the triangular TMD lateral heterostructures. Figure 7a shows the strain distribution of the triangular MoS₂–WSe₂ lateral heterostructure, where the MoS₂(WSe₂) region is stretched (compressed). There is obvious strain concentration at the three corners of the triangular MoS₂ area. Figure 7b shows the buckling shape of the triangular MoS₂–WSe₂ lateral heterostructure. The misfit strain-induced buckling also takes place for the triangular MoS₂–WSe₂ lateral heterostructure with more heteros as shown in Fig. 7c, d. Figure 8 shows the misfit strain-induced buckling instability of the triangular WSe₂–MoS₂ lateral heterostructure, where the sequence of MoS₂ and WSe₂ is exchanged as compared with the structure shown in Fig. 7.

4. Conclusion

In conclusion, we have performed molecular dynamics simulations to study the misfit strain-induced buckling phenomena in the MoS₂–WSe₂, MoS₂–WTe₂, MoS₂–MoSe₂, and MoS₂–MoTe₂ lateral heterostructures, where the atomic interactions for these multiple-component systems are described by

the SW potential. We explored the strain distribution within the heterostructure, which is consistent with the experiment. We found that the misfit strain can cause buckling of the TMD with larger lattice constants in the lateral heterostructure, due to the atomic-thick nature of TMDs. The misfit strain-induced buckling is quite general for TMD lateral heterostructures of different constitutions and different hetero-patterns.

Acknowledgements. The work is supported by the Recruitment Program of Global Youth Experts of China, the National Natural Science Foundation of China (NSFC) under Grant No. 11504225, and the Innovation Program of Shanghai Municipal Education Commission under Grant No. 2017-01-07-00-09-E00019.

References

- [1] Huang C, Wu S, Sanchez AM, Peters JJ, Beanland R, Ross JS. Lateral heterojunctions within monolayer MoSe₂–WSe₂ semiconductors. *Nat Mater.* 2014;13(12):1096.
- [2] Gong Y, Lin J, Wang X, Shi G, Lei S, Lin Z. Vertical and in-plane heterostructures from WS₂/MoS₂ monolayers. *Nat Mater.* 2014;13(12):1135.
- [3] Zhang X-Q, Lin C-H, Tseng Y-W, Huang K-H, Lee Y-H. Synthesis of lateral heterostructures of semiconducting atomic layers. *Nano Lett.* 2014;15(1):410–5.
- [4] Duan X, Wang C, Shaw JC, Cheng R, Chen Y, Li H. Lateral epitaxial growth of two-dimensional layered semiconductor heterojunctions. *Nat Nanotechnol.* 2014;9(12):1024.
- [5] Chen K, Wan X, Wen J, Xie W, Kang Z, Zeng X. Electronic properties of MoS₂–WS₂ heterostructures synthesized with two-step lateral epitaxial strategy. *ACS Nano.* 2015;9(10):9868–76.
- [6] Chen K, Wan X, Xie W, Wen J, Kang Z, Zeng X. Lateral built-in potential of monolayer MoS₂–WS₂-in-plane heterostructures by a shortcut growth strategy. *Adv Mater.* 2015;27(41):6431–7.
- [7] Gong Y, Lei S, Ye G, Li B, He Y, Keyshar K. Two-step growth of two-dimensional WSe₂/MoSe₂ heterostructures. *Nano Lett.* 2015;15(9):6135–41.
- [8] Chen J, Zhou W, Tang W, Tian B, Zhao X, Xu H. Lateral epitaxy of atomically sharp WSe₂/WS₂ heterojunctions on silicon dioxide substrates. *Chem Mater.* 2016;28(20):7194–7.
- [9] Ling X, Lin Y, Ma Q, Wang Z, Song Y, Yu L. Parallel stitching of 2D materials. *Adv Mater.* 2016;28(12):2322–9.
- [10] Liu B, Ma Y, Zhang A, Chen L, Abbas AN, Liu Y. High-performance WSe₂ field-effect transistors via controlled formation of in-plane heterojunctions. *ACS Nano.* 2016;10(5):5153–60.
- [11] Son Y, Li M-Y, Cheng C-C, Wei K-H, Liu P, Wang QH. Observation of switchable photoresponse of a monolayer WSe₂–MoS₂ lateral heterostructure via photocurrent spectral atomic force microscopic imaging. *Nano Lett.* 2016;16(6):3571–7.
- [12] Chen X, Qiu Y, Yang H, Liu G, Zheng W, Feng W. In-plane mosaic potential growth of large-area 2D layered semiconductors MoS₂–MoSe₂ lateral heterostructures and photodetector application. *ACS Appl Mater Interfaces.* 2017;9(2):1684–91.
- [13] Li MY, Pu J, Huang JK, Miyauchi Y, Matsuda K, Takenobu T. Self-aligned and scalable growth of monolayer WSe₂–MoS₂ lateral heterojunctions. *Adv Funct Mater.* 2018;28(17):1706860.
- [14] Sahoo PK, Memaran S, Xin Y, Balicas L, Gutiérrez HR. One-pot growth of two-dimensional lateral heterostructures via sequential edge-epitaxy. *Nature.* 2018;553(7686):63.
- [15] Li M-Y, Shi Y, Cheng C-C, Lu L-S, Lin Y-C, Tang H-L. Epitaxial growth of a monolayer WSe₂–MoS₂ lateral pn junction with an atomically sharp interface. *Science.* 2015;349(6247):524–8.
- [16] Zhang Z, Chen P, Duan X, Zang K, Luo J, Duan X. Robust epitaxial growth of two-dimensional heterostructures, multiheterostructures, and superlattices. *Science.* 2017;357:eaan6814.
- [17] Bogaert K, Liu S, Chesin J, Titow D, Gradečak S, Garaj S. Diffusion-mediated synthesis of MoS₂/WS₂ lateral heterostructures. *Nano Lett.* 2016;16(8):5129–34.
- [18] Li H, Wu X, Liu H, Zheng B, Zhang Q, Zhu X. Composition-modulated two-dimensional semiconductor lateral heterostructures via layer-selected atomic substitution. *ACS Nano.* 2016;11(1):961–7.
- [19] Mahjouri-Samani M, Lin M-W, Wang K, Lupini AR, Lee J, Basile L. Patterned arrays of lateral heterojunctions within monolayer two-dimensional semiconductors. *Nat Commun.* 2015;6:7749.
- [20] Li H, Li P, Huang J-K, Li M-Y, Yang C-W, Shi Y. Laterally stitched heterostructures of transition metal dichalcogenide: chemical vapor deposition growth on lithographically patterned area. *ACS Nano.* 2016;10(11):10516–23.
- [21] Ullah F, Sim Y, Le CT, Seong M-J, Jang JI, Rhim SH. Growth and simultaneous valleys manipulation of two-dimensional MoSe₂–WSe₂ lateral heterostructure. *ACS Nano.* 2017;11(9):8822–9.
- [22] Kobayashi Y, Mori S, Maniwa Y, Miyata Y. Bandgap-tunable lateral and vertical heterostructures based on monolayer Mo_{1-x}W_xS₂ alloys. *Nano Res.* 2015;8(10):3261–71.

- [23] Zhang W, Li X, Jiang T, Song J, Lin Y, Zhu L. CVD synthesis of Mo_(1-x)W_xS₂ and MoS₂(1-x)Se_{2x} alloy monolayers aimed at tuning the bandgap of molybdenum disulfide. *Nanoscale*. 2015;7(32):13554–60.
- [24] Yoshida S, Kobayashi Y, Sakurada R, Mori S, Miyata Y, Mogi H. Microscopic basis for the band engineering of Mo_{1-x}W_xS₂-based heterojunction. *Sci Rep*. 2015;5:14808.
- [25] Duan X, Wang C, Fan Z, Hao G, Kou L, Halim U. Synthesis of WS₂ × Se₂₋₂ × alloy nanosheets with composition-tunable electronic properties. *Nano Lett*. 2015;16(1):264–9.
- [26] Liu X, Wu J, Yu W, Chen L, Huang Z, Jiang H. Monolayer W_xMo_{1-x}S₂ grown by atmospheric pressure chemical vapor deposition: bandgap engineering and field effect transistors. *Adv Funct Mater*. 2017;27(13):1606469.
- [27] Aslan OB, Datye IM, Mleczko MJ, Sze Cheung K, Krylyuk S, Bruma A. Probing the optical properties and strain-tuning of ultrathin Mo_{1-x}W_xTe₂. *Nano Lett*. 2018;18(4):2485–91.
- [28] Apte A, Kochat V, Rajak P, Krishnamoorthy A, Manimunda P, Hachtel JA. Structural phase transformation in strained monolayer MoWSe₂ alloy. *ACS Nano*. 2018;12(4):3468–76.
- [29] Li H, Zhang Q, Duan X, Wu X, Fan X, Zhu X. Lateral growth of composition graded atomic layer MoS₂(1-x)Se₂ × nanosheets. *J Am Chem Soc*. 2015;137(16):5284–7.
- [30] Zheng S, Sun L, Yin T, Dubrovkin AM, Liu F, Liu Z. Monolayers of W_xMo_{1-x}S₂ alloy heterostructure with in-plane composition variations. *Appl Phys Lett*. 2015;106(6):063113.
- [31] Wu X, Li H, Liu H, Zhuang X, Wang X, Fan X. Spatially composition-modulated two-dimensional WS₂ × Se₂(1-x) nanosheets. *Nanoscale*. 2017;9(14):4707–12.
- [32] Li Z, Zheng J, Zhang Y, Zheng C, Woon W-Y, Chuang M-C. Synthesis of ultrathin composition graded doped lateral WSe₂/WS₂ heterostructures. *ACS Appl Mater Interfaces*. 2017;9(39):34204–12.
- [33] Xie S, Tu L, Han Y, Huang L, Kang K, Lao KU. Coherent, atomically thin transition-metal dichalcogenide superlattices with engineered strain. *Science*. 2018;359(6380):1131–6.
- [34] Zhang C, Li M-Y, Tersoff J, Han Y, Su Y, Li L-J. Strain distributions and their influence on electronic structures of WSe₂-MoS₂ laterally strained heterojunctions. *Nat Nanotechnol*. 2018;13(2):152.
- [35] Alred JM, Zhang Z, Hu Z, Yakobson BI. Interface-induced warping in hybrid two-dimensional materials. *Nano Res*. 2015;8(6):2015.
- [36] Shi Z, Zhang Q, Schwingenschlögl U. Alloying as a route to monolayer transition metal dichalcogenides with improved optoelectronic performance: Mo_{(S1-x)Se x}2 and Mo_{1-y}W_yS₂. *ACS Appl Energy Mater*. 2018;1(5):2208–14.
- [37] Wei W, Dai Y, Niu C, Huang B. Controlling the electronic structures and properties of in-plane transition-metal dichalcogenides quantum wells. *Sci Rep*. 2015;5:17578.
- [38] Wei W, Dai Y, Sun Q, Yin N, Han S, Huang B. Electronic structures of in-plane two-dimensional transition-metal dichalcogenide heterostructures. *Phys Chem Chem Phys*. 2015;17(43):29380–6.
- [39] Guo Y, Robertson J. Band engineering in transition metal dichalcogenides: stacked versus lateral heterostructures. *Appl Phys Lett*. 2016;108(23):233104.
- [40] Wei W, Dai Y, Huang B. In-plane interfacing effects of two-dimensional transition-metal dichalcogenide heterostructures. *Phys Chem Chem Phys*. 2016;18(23):15632–8.
- [41] Zhang J, Xie W, Zhao J, Zhang S. Band alignment of two-dimensional lateral heterostructures. *2D Mater*. 2016;4(1):015038.
- [42] Wei W, Dai Y, Huang B. Straintronics in two-dimensional in-plane heterostructures of transition-metal dichalcogenides. *Phys Chem Chem Phys*. 2016;19(1):663–72.
- [43] Aras M, Kılıç Ç, Ciraci S. Lateral and vertical heterostructures of transition metal dichalcogenides. *J Phys Chem C*. 2018;122(3):1547–55.
- [44] Kang J, Sahin H, Peeters FOM. Tuning carrier confinement in the MoS₂/WS₂ lateral heterostructure. *J Phys Chem C*. 2015;119(17):9580–6.
- [45] An Y, Zhang M, Wu D, Fu Z, Wang K. The electronic transport properties of transition-metal dichalcogenide lateral heterojunctions. *J Mater Chem*. 2016;4(46):10962–6.
- [46] Yang Z, Pan J, Liu Q, Wu N, Hu M, Ouyang F. Electronic structures and transport properties of a MoS₂-NbS₂ nanoribbon lateral heterostructure. *Phys Chem Chem Phys*. 2017;19(2):1303–10.
- [47] Cao Z, Harb M, Lardhi S, Cavallo L. Impact of interfacial defects on the properties of monolayer transition metal dichalcogenide lateral heterojunctions. *J Phys Chem Lett*. 2017;8(7):1664–9.
- [48] Sun J, Lin N, Ren H, Tang C, Yang L, Zhao X. Gas adsorption on MoS₂/WS₂ in-plane heterojunctions and the I-V response: a first principles study. *RSC Adv*. 2016;6(21):17494–503.
- [49] Yang Y, Fang WH, Long R. Disparity in photoexcitation dynamics between vertical and lateral MoS₂/WSe₂ heterojunctions: time-domain simulation emphasizes the importance of donor-acceptor interaction and band alignment. *J Phys Chem Lett*. 2017;8:5771–8.

- [50] Sun Q, Dai Y, Ma Y, Yin N, Wei W, Yu L. Design of lateral heterostructure from arsenene and antimonene. *2D Mater.* 2016;3(3):035017.
- [51] Jin H, Li J, Wang B, Yu Y, Wan L, Xu F. Electronics and optoelectronics of lateral heterostructures within monolayer indium monochalcogenides. *J Mater Chem C.* 2016;4(47):11253–60.
- [52] Leenaerts O, Vercauteren S, Schoeters B, Partoens B. System-size dependent band alignment in lateral two-dimensional heterostructures. *2D Mater.* 2016;3(2):025012.
- [53] Leenaerts O, Vercauteren S, Partoens B. Band alignment of lateral two-dimensional heterostructures with a transverse dipole. *Appl Phys Lett.* 2017;110(18):181602.
- [54] Cheng K, Guo Y, Han N, Su Y, Zhang J, Zhao J. Lateral heterostructures of monolayer group-IV monochalcogenides: band alignment and electronic properties. *J Mater Chem C.* 2017;5(15):3788–95.
- [55] Sun Q, Dai Y, Niu C, Ma Y, Wei W, Yu L. Lateral topological crystalline insulator heterostructure. *2D Mater.* 2017;4(2):025038.
- [56] Sun Q, Dai Y, Yin N, Yu L, Ma Y, Wei W. Two-dimensional square transition metal dichalcogenides with lateral heterostructures. *Nano Res.* 2017;10(11):3909–19.
- [57] Yuan J, Yu N, Wang J, Xue K-H, Miao X. Design lateral heterostructure of monolayer ZrS₂ and HfS₂ from first principles calculations. *Appl Surf Sci.* 2018;436:919–26.
- [58] Jiang J-W, Zhou Y-P. Parameterization of Stillinger–Weber potential for two-dimensional atomic crystals. *Handbook of Stillinger–Weber potential parameters for two-dimensional atomic crystals.* The Hague: InTech; 2017.
- [59] Jiang J-W. Parametrization of Stillinger–Weber potential based on valence force field model: application to single-layer MoS₂ and black phosphorus. *Nanotechnology.* 2015;26(31):315706.
- [60] Nosé S. A unified formulation of the constant temperature molecular dynamics methods. *J Chem Phys.* 1984;81(1):511–9.
- [61] Hoover WG. Canonical dynamics: equilibrium phase-space distributions. *Phys Rev A.* 1985;31(3):1695.
- [62] Plimpton S. Fast parallel algorithms for short-range molecular dynamics. *J Comput Phys.* 1995;117(1):1–19.
- [63] Stukowski A. Visualization and analysis of atomistic simulation data with OVITO—the Open Visualization Tool. *Model Simul Mater Sci Eng.* 2009;18(1):015012.
- [64] Kushima A, Qian X, Zhao P, Zhang S, Li J. Ripples in van der Waals Layers. *Nano Lett.* 2015;15(2):1302–8.
- [65] Zhou Y-P, Jiang J-W. Molecular dynamics simulations for mechanical properties of borophene: parameterization of valence force field model and Stillinger–Weber potential. *Sci Rep.* 2017;7:45516.

Appendix: Modification for LAMMPS

We point out one necessary modification for the three-body SW potential implemented in LAMMPS. More details on this modification can be found from our earlier work [65]. Overall, the modification is done in two steps.

- 1) First, find the following line in the pair sw.cpp source file,
`delcs = cs - paramijk->costheta;`
- 2) Second, insert the following new lines after the above line,

```

if(fabs(delcs) <= 0.25)
{
    delcs = delcs;
} else if(fabs(delcs) < 0.35)
{
    delcs = delcs * (0.5+0.5*sin(3.142*(delcs-0.25)/(0.35-0.25)+0.5*3.142));
}
else
{
    delcs = 0.0;
}
```

Then, recompile the LAMMPS package. The recompiled LAMMPS executable file can be used to simulate materials with inequivalent angles around each atom (like TMDs in the present work) using the SW potential. This modification does not affect other simulations with LAMMPS.